

Higher-order Topological Hyperbolic Lattices

Yu-Liang Tao¹ and Yong Xu^{1*}

¹Center for Quantum Information, IIIS, Tsinghua University, Beijing 100084, People's Republic of China

A hyperbolic lattice allows for any p -fold rotational symmetry, in stark contrast to a two-dimensional crystalline material, where only twofold, threefold, fourfold or sixfold rotational symmetry is permitted. This unique feature motivates us to ask whether the enriched rotational symmetry in a hyperbolic lattice can lead to any new topological phases beyond a crystalline material. Here, by constructing and exploring tight-binding models in hyperbolic lattices, we theoretically demonstrate the existence of higher-order topological phases in hyperbolic lattices with eight-fold, twelve-fold, sixteen-fold or twenty-fold rotational symmetry, which is not allowed in a crystalline lattice. Since such models respect the combination of time-reversal symmetry and p -fold ($p = 8, 12, 16$ or 20) rotational symmetry, p zero-energy corner modes are protected. For the hyperbolic $\{8,3\}$ lattice, we find a gapped, a gapless and a reentrant gapped higher-order topological hyperbolic phases. The reentrant phase arises from finite-size effects, which open the gap of edge states while leave the gap of corner modes unchanged. Our results thus open the door to studying higher-order topological phases in hyperbolic lattices.

Recently, hyperbolic lattices have been experimentally realized in circuit quantum electrodynamics [1] and electric circuits [2–4], igniting great interest in study of various properties of hyperbolic lattices [5–17], such as topological properties, hyperbolic band theory and flat band properties. Different from a hyperbolic lattice, it is a well-known fact that only twofold, threefold, fourfold or sixfold rotational symmetry is permitted in two-dimensional (2D) crystalline materials. In other words, one can only use regular p -sided polygons with $p = 3, 4$ or 6 to tessellate the 2D Euclidean plane. However, for a hyperbolic lattice with constant negative curvature, such a restriction is lifted so that one can use regular p -gons for any integer $p > 2$ to tessellate a hyperbolic plane [see Fig. 1(a)]. As a result, any p -fold rotational symmetry can be realized in a hyperbolic lattice. This leads to a natural question of whether the enriched rotational symmetry of a hyperbolic lattice will result in any new topological phases beyond crystalline systems.

Recent generalizations of topological phases to the higher-order case provide us with an opportunity to study the effects of the enriched rotational symmetry. Different from the conventional first-order topological system, such a topological phase supports $(n - m)$ -dimensional ($1 < m \leq n$) gapless boundary modes for an n -dimensional system [18–40]. For instance, a two-dimensional (2D) second-order topological insulator may support two, four or six zero-energy corner modes [18, 30, 36]. Since the number of corner modes is closely related to the crystalline symmetry of a system, one thus may wonder whether the new rotational symmetry in hyperbolic lattices can allow for the existence of new higher-order topological phases that cannot exist in a crystalline material.

In this work, we theoretically demonstrate the existence of higher-order topological phases in hyperbolic lattices with eight-fold, twelve-fold, sixteen-fold or twenty-fold rotational symmetry by constructing and exploring tight-binding models on the lattices. Such Hamiltonians

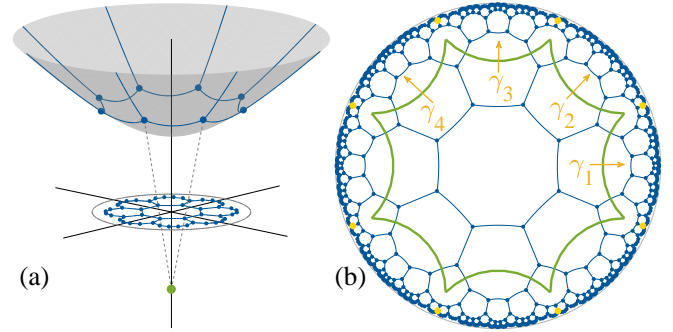


FIG. 1. (a) Projection of a hyperbolic $\{8,3\}$ lattice onto a Poincaré disk. Regular hyperbolic octagons are used to tessellate the hyperbolic plane (described by the equation $z^2 - x^2 - y^2 = 1$) so that each lattice site is connected to three neighboring sites through the geodesics on the hyperbolic plane. The lattices on the hyperbolic plane are projected onto the unit disk on the $z = 0$ plane through a line connecting points on the lattices to the point at $(0, 0, -1)$, leading to the Poincaré disk model. In fact, one can achieve the tessellation through applying translational operations (generated by four generators $\gamma_1, \dots, \gamma_4$) to a unit cell [the region enclosed by the green curve in (b)]. Such translational operations form a group that is non-Abelian. (b) The Poincaré disk model for the hyperbolic $\{8,3\}$ lattice. Solid yellow circles describe the corner modes of a higher-order topological phase on the hyperbolic lattice.

respect the combination of time-reversal symmetry and p -fold ($p = 8, 12, 16$ or 20) rotational symmetry, which is not allowed in a crystalline lattice. While a quasicrystal may allow for the eight-fold or twelve-fold rotational symmetry, to the best of our knowledge, it is unclear whether sixteen-fold or twenty-fold rotational symmetry can occur there [41]. For clarify of presentation, we mainly focus on a hyperbolic $\{8,3\}$ lattice where regular 8-gons are used to tessellate a hyperbolic plane such that each lattice site is connected to three neighboring sites [see Fig. 1(b)]. Note that for the Euclidean plane, only $\{3,6\}$, $\{4,4\}$ and

$\{6, 3\}$ lattices can achieve the tessellation. For the hyperbolic $\{8, 3\}$ lattice, we find a gapped and a gapless higher-order topological hyperbolic phase by numerically computing the quadrupole moment and energy band properties of a four-dimensional (4D) momentum-space Hamiltonian based on the hyperbolic band theory [8]. We further directly diagonalize the Hamiltonian in real space under open boundary conditions, illustrating the existence of zero-energy modes localized at eight corners in both gapped and gapless higher-order topological phases (which refer to the cases with gapped or gapless bulk and edge states, respectively). Interestingly, the real space results also show a reentrant gapped topological phase with zero-energy corner modes, which is different from the momentum space case. We find that the size and edge energy gap of this region decrease with the increase of the system size, suggesting that the phase may arise from finite-size effects. In fact, the phase occurs because the edge states are more sensitive to finite-size effects than the corner states. Such a phenomenon is in stark contrast to our conventional wisdom that finite-size effects usually open the gap of boundary modes, thereby destroying a topological phase. Our results thus demonstrate much richer higher-order topological phenomena in hyperbolic lattices. Finally, we show the existence of twelve, sixteen or twenty zero-energy corner modes in a hyperbolic lattice with the corresponding rotational symmetry.

Model Hamiltonian.—To demonstrate the existence of higher-order topological phases in hyperbolic lattices, we start by constructing the following tight-binding model Hamiltonian in a hyperbolic $\{p, q\}$ lattice described by the Poincaré disk model [see Fig. 1(b)],

$$H = \sum_{\alpha, \beta} \left[\sum_i m |i\alpha\rangle [\tau_z \sigma_0]_{\alpha\beta} \langle i\beta| + \sum_{\langle i, j \rangle} |i\alpha\rangle [T(\theta_{ij})]_{\alpha\beta} \langle j\beta| \right], \quad (1)$$

where $|i\alpha\rangle$ denotes the state of the α th degree of freedom at the site i in the Poincaré disk. At each site, there are four degrees of freedom, and $\{\tau_\nu\}$ and $\{\sigma_\nu\}$ with $\nu = x, y, z$ are two sets of Pauli matrices that act on these degrees of freedom. In the above Hamiltonian, the first term $m\tau_z\sigma_0$ describes the on-site energy, and the second term depicts the hopping between two neighboring connected sites with the hopping matrix $T(\theta_{ij}) = [t_0\tau_z\sigma_0 - it_1(\cos\theta_{ij}\tau_x\sigma_x + \sin\theta_{ij}\tau_x\sigma_y) + g\cos(p\theta_{ij}/2)\tau_y\sigma_0]/2$, where θ_{ij} is the polar angle of the vector from the site i to site j in the disk. Note that p should be an integer multiple of 4 to ensure that the Hamiltonian is Hermitian. In the following, we will set the system parameters $t_0 = t_1 = 1$ as the units of energy.

When $g = 0$, the system respects in-plane mirror symmetry $M_1 = \tau_z\sigma_z$, time-reversal symmetry $T = i\sigma_y\kappa$ where κ is the complex conjugate operator, chiral symmetry $\Gamma = \tau_x\sigma_z$, and thus particle-hole symmetry $\Xi = \tau_x\sigma_x\kappa$. Owing to the p -fold rotational symmetry

about the z axis preserved by the hyperbolic lattice, the Hamiltonian also respects the p -fold rotational symmetry $C_p = \tau_0 e^{-i\frac{z}{p}\sigma_z} R_p$ where $R_p|i\alpha\rangle \equiv |g_p(i)\alpha\rangle$ with $g_p(i)$ rotating the lattice site i by an angle $2\pi/p$ about the z axis. With these internal symmetry, the system belongs to the DIII class corresponding to a \mathbb{Z}_2 topological insulator whose nontrivial phase exhibits helical edge modes. To generate a higher-order phase with corner modes, we add the term $g\cos(p\theta_{ij}/2)\tau_y\sigma_0$ to break the time-reversal symmetry so as to open the gap of the helical modes at a boundary; this term thus acts as an edge mass term. As this term changes its sign once θ_{ij} increases by $2\pi/p$, a corner state may arise at the location where the mass flips its sign. Since the change of sign occurs p times, total p corner modes may appear. While the term also breaks the C_p symmetry, the combination of T and C_p symmetry is still conserved, that is, $[C_p T, H] = 0$. The symmetry ensures that the number of corner modes must be an integer multiple of p given the fact that if there is a zero-energy corner mode $|\psi_c\rangle$ mainly localized at \mathbf{r} , then $C_p T|\psi_c\rangle$ is also a zero-energy corner mode mainly localized at $g_p(\mathbf{r})$.

Momentum-space topological invariant.—We now consider the hyperbolic $\{8, 3\}$ lattice. The lattice can be constructed by applying translational operations (generated by four generators $\gamma_1, \dots, \gamma_4$) to the 16-site unit cell enclosed by the blue curve, as shown in Fig. 1(b). We first employ the twisted boundary conditions to construct the momentum-space Bloch Hamiltonian based on the hyperbolic band theory [8, 11, 17]. In the Hamiltonian, the hopping between two sites in two different unit cells which are connected by a translation operator γ_i should carry an extra phase term e^{ik_i} . We thus obtain a 64×64 Hamiltonian $H(\mathbf{k}) = H(k_1, k_2, k_3, k_4)$ in a four-dimensional Brillouin zone with $k_i \in [0, 2\pi]$ for $i = 1, \dots, 4$.

While time-reversal symmetry is broken in the Hamiltonian H , chiral symmetry is still preserved so that $H(\mathbf{k})$ respects chiral symmetry. In light of the fact that the quadrupole moment [42, 43] is protected to be quantized by chiral symmetry [38, 39], we can utilize the quadrupole moment to characterize the topological property of $H(\mathbf{k})$ spanned by two of the four momenta. Specifically, one can regard $H(\mathbf{k})$ spanned by k_i and k_j ($i, j \in 1, \dots, 4$ and $i \neq j$) with the other two momenta $k_{\bar{i}}$ and $k_{\bar{j}}$ fixed as the momentum-space version of a Hamiltonian H_s in an $L \times L$ square lattice. The quadrupole moment for the occupied states is defined as [38]

$$Q_{ij}(k_{\bar{i}}, k_{\bar{j}}) = \left[\frac{1}{2\pi} \text{Im} \log \det(U_o^\dagger \hat{D} U_o) - Q_o \right] \text{mod } 1, \quad (2)$$

where $U_o = (|\psi_1\rangle, |\psi_2\rangle, \dots, |\psi_{n_c}\rangle)$ with $|\psi_j\rangle$ being the j th occupied eigenstate of H_s (one of $n_c = 32L^2$ occupied states), and $\hat{D} = \text{diag} \left\{ e^{2\pi i x_j y_j / L^2} \right\}_{j=1}^{64L^2}$ with (x_j, y_j) denoting the square position of the j th lattice site. Here, Q_o

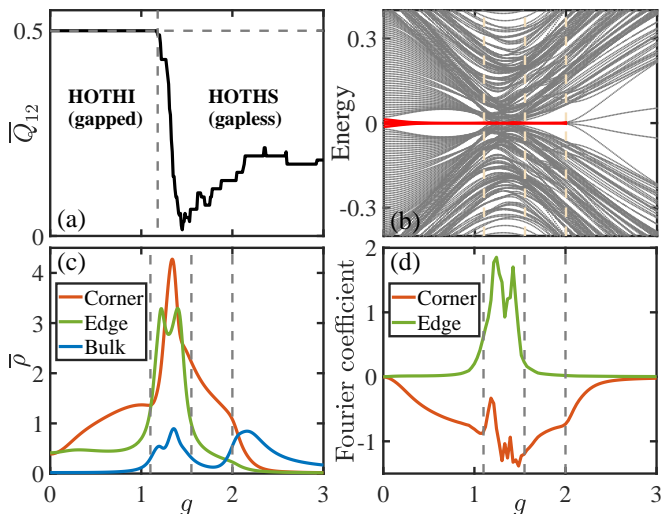


FIG. 2. Topological and band properties of a hyperbolic $\{8, 3\}$ lattice. (a) \bar{Q}_{12} as a function of g . Two different phases are identified: higher-order topological hyperbolic insulator (HOTH) and higher-order topological hyperbolic semimetal (HOTHs). (b) The energy spectrum of the tight-binding Hamiltonian in Eq. (1) under open boundary conditions with respect to g . Red lines highlight the zero-energy corner modes. (c) Zero-energy average DOS defined as $\bar{\rho} = (1/N) \sum_{\mathbf{r} \in S} \rho(E=0, \mathbf{r})$ at corner (red line), edge (green line) and bulk (blue line) sites. For the corner (edge) one, S is a set consisting of eleven (sixty) sites on the boundary near a corner (the center of an edge). For the bulk one, S contains sixteen sites located in the central unit cell. N denotes the number of elements in S . (d) The Fourier coefficient b of the corner (red line) and edge (green line) local DOS with respect to g (see the text on how to evaluate b). In (b)-(d), the system has 746 sites, and four distinct phases are separated by three dashed vertical lines. Here, $m = 0.8$.

is the contribution from the background positive charge distribution.

To distinguish between an insulating phase and a semimetal phase, we calculate the average quadrupole moment over all fixed momenta $(k_{\bar{i}}, k_{\bar{j}})$

$$\bar{Q}_{ij} = \frac{1}{(2\pi)^2} \int dk_{\bar{i}} dk_{\bar{j}} Q_{ij}(k_{\bar{i}}, k_{\bar{j}}). \quad (3)$$

The system respects C_8M_1 symmetry, that is, $U_{C_8M_1} H(k_1, k_2, k_3, k_4) (U_{C_8M_1})^{-1} = H(-k_4, k_1, k_2, k_3)$. It follows that \bar{Q}_{ij} should satisfy the following relations (see Supplemental Material Sec. S-1 for proof):

$$\begin{aligned} \bar{Q}_{12} = \bar{Q}_{23} = \bar{Q}_{34} = \bar{Q}_{41} \\ \text{and} \quad \bar{Q}_{13} = \bar{Q}_{24}. \end{aligned} \quad (4)$$

We find that \bar{Q}_{13} is always equal to zero and thus use \bar{Q}_{12} to characterize the topological property.

The average quadrupole moment illustrates a sharp decline from a quantized value of 0.5 to a nonzero fractional value as g increases as shown in Fig. 2(a), indicating the presence of two distinct phases. One phase

is a higher-order topological hyperbolic insulator with $\bar{Q}_{12} = 0.5$. The other one is a higher-order topological hyperbolic semimetal with vanishing energy gap in the 4D momentum space [44]. In fact, there are several degenerate nodes in momentum space. In the Brillouin zone spanned by (k_3, k_4) , a part has the quadrupole moment \bar{Q}_{12} of 0.5 and the other part has zero \bar{Q}_{12} , leading to a fractional value of the average quadrupole moment (see Supplemental Material Sec. S-2 for detailed discussion). The existence of the gapless phase is in stark contrast to the higher-order phase on Euclidean square $\{4, 4\}$ lattices where the system is always gapped as we increase the term that breaks the time-reversal symmetry [18, 24] (also see Supplemental Material Sec. S-3).

Real space topological and band properties.—The hyperbolic band theory neglects the states representing the higher-dimensional representation of the non-Abelian translational group in a hyperbolic lattice. Thus, to obtain all eigenenergy information, one needs to calculate the eigenenergies of the Hamiltonian in Eq. (1) in real space under open boundary conditions. In addition, such calculations allow us to identify the consequence of the higher-order bulk topological properties, that is, the existence of zero-energy corner modes. To illustrate the existence of these modes, we calculate the local density of states (DOS) defined as

$$\rho(E, \mathbf{r}) = \sum_{n,i} \delta(E - E_n) |\Psi_{E_n,i}(\mathbf{r})|^2, \quad (5)$$

based on the numerically calculated eigenstate $\Psi_{E_n,i}(\mathbf{r})$ (the i th component of the eigenstate at site \mathbf{r}) corresponding to the n th eigenenergy E_n .

In Fig. 2(b), we plot the energy spectrum of the hyperbolic lattice as a function of g in real space for open boundaries with $m = 0.8$. We find three regions with zero-energy states separated by three vertical dashed lines. The first region ($0 < g \lesssim 1.1$) corresponds to a higher-order topological insulating phase with eight zero-energy modes localized at corners as shown in Fig. 3(a). More quantitatively, we see in Fig. 2(c) that in this region the average local DOS at the corner is finite while the one in the bulk almost vanishes. When $g = 0$, the system is in the first-order topological phase, and thus the gapless edge states are almost equally distributed on the edge and corner sites. As we increase g , the energy gap at the edge is opened, leading to the appearance of corner modes, reflected by the increase of the average local DOS at the corner.

As we further increase g , the energy spectrum in Fig. 2(b) becomes continuous near zero, and the number of zero-energy states is more than eight, leading to a gapless higher-order topological phase ($1.1 \lesssim g \lesssim 1.55$). The phase corresponds to the higher-order topological semimetal phase identified via the hyperbolic band theory. Local DOS at zero energy in Fig. 3(b) exhibits the distribution mainly localized at edges and corners (here

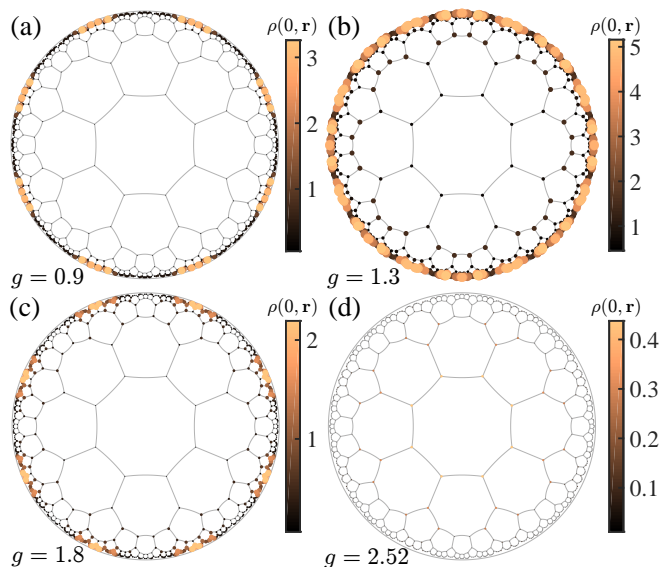


FIG. 3. The local DOS $\rho(E, \mathbf{r})$ at zero energy. Each figure corresponds to a typical local DOS for each phase shown in Fig. 2(b). (a)-(c) illustrate the existence of eight corner modes.

an edge represents the boundary sites between two nearest neighboring corners), implying that the gapless modes are mainly comprised of corner and edge modes. Such a fact is also revealed by a significant rise of the average local DOS at the corner and edge when we enter into this regime [see Fig. 2(c)].

To further confirm the existence of zero-energy corner modes in the gapless regime, we perform the Fourier analysis of the zero-energy local DOS at the boundary of the hyperbolic lattice. The local DOS $\rho(\theta)$ is a function of the polar angle θ in the Poincaré disk for each site at the boundary. Because of the C_8T symmetry, it is a periodic function of θ with the period of $\pi/4$, i.e., $\rho(\theta + \pi/4) = \rho(\theta)$. In our case as shown in Fig. 1, the positions of corners refer to the boundary sites at $\theta_c = \pi/8 + n\pi/4$ with $n = 0, 1, \dots, 7$. The boundary sites between two nearest neighboring corners is thus referred to as an edge. To identify whether an eigenstate near the zero energy is a corner mode, we expand the density of the eigenstate in a Fourier series up to the first order, that is, $|\Psi_{E_n}|^2 = a[1 + b \cos(8\theta)]$. If $b < 0$, then the density takes a maximum value at corners $\theta = \theta_c$; if $b > 0$, the maximum occurs at the center of each edge, i.e., $\theta = n\pi/4$ with $n = 0, 1, \dots, 7$. We thus classify the state with $b < 0$ ($b > 0$) as a corner (edge) mode. We then use the classified corner (edge) modes to calculate the corresponding local DOS and the Fourier coefficient b in a Fourier series of the local DOS as shown in Fig. 2(d). In the region $0 < g \lesssim 2$, the Fourier coefficient for the corner local DOS is finite and negative, consistent with our previous results indicating the existence of zero-energy corner modes. However, for the edge local DOS,

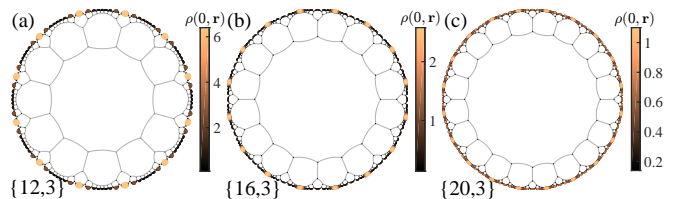


FIG. 4. The local DOS at zero energy for hyperbolic (a) $\{12, 3\}$ lattice with $m = 0.9$ and $g = 0.8$, (b) $\{16, 3\}$ lattice with $m = 0.975$ and $g = 0.57$, and (c) $\{20, 3\}$ lattice with $m = 1$ and $g = 0.6$.

the coefficient vanishes in the gapped region, indicating the absence of edge modes in these regions. In the gapless region, it is positive and finite, implying the presence of edge states. We thus conclude the coexistence of edge states and corner states in the gapless region.

In Fig. 2(b), we also see that with the further increase of g until 2, the energy spectrum becomes gapped again with eight zero-energy states separated from the other states. The phase arises because of the overlap between edge wave functions, leading to the energy gap opening of the edge states. Such an overlap is reflected by the sudden drop of the proportion of edge states on the boundary with respect to g [see Fig. S2(a) in Supplemental Material]. In other words, the finite-size effect opens the gap of the edge wave functions, leaving the corner modes at zero energy [also evidenced by the zero-energy local DOS in Fig. 3(c)]. The finite-size effect will be reduced by increasing the system size so that the gapless regime and the edge energy gap become smaller (see Supplemental Material Sec. S-3). We note that such a finite-size effect facilitates the formation of a gapped phase with corner modes, which is different from the traditional case where finite-size effects usually destroy a topological phase. In addition, when $g > 2$, zero-energy corner modes bifurcate into four branches away from zero energy, and no corner states are observed in this phase [see Fig. 3(d)].

We also examine the stability of the higher-order topological phases by introducing weak uniformly distributed random on-site disorder, which respects the chiral symmetry and C_pT symmetry. We find that these phases are stable against the weak disorder (see Supplemental Material Sec. S-4).

Higher-order topological phases with twelve, sixteen or twenty corner modes.—We now proceed to study the higher-order topological phase in a hyperbolic lattice respecting twelve-fold, sixteen-fold or twenty-fold rotational symmetry by constructing the Hamiltonian in hyperbolic $\{12, 3\}$, $\{16, 3\}$, or $\{20, 3\}$ lattices. Such Hamiltonians respect chiral symmetry and the corresponding C_pT symmetry with $p = 12, 16$, or 20. Figure 4 illustrates the local DOS at zero energy in the Poincaré disk, indicating the existence of twelve, sixteen and twenty corner modes, respectively. All these phases arise from the

allowed rotational symmetry of a hyperbolic lattice, and thus cannot exist in a crystalline material. Even in a quasicrystal, it is unclear whether sixteen-fold or twenty-fold rotational symmetry can occur, to the best of our knowledge [41].

In summary, we have theoretically predicted higher-order topological phases in hyperbolic lattices with eight-fold, twelve-fold, sixteen-fold or twenty-fold rotational symmetry, which have eight, twelve, sixteen and twenty corner modes, respectively. Such phases are not allowed in a crystalline material. For the hyperbolic $\{8, 3\}$ lattices, we identify a gapped, a gapless and a reentrant gapped higher-order topological phases. The gapped topological phases can be characterized by a corner charge (see Supplemental Material Sec. S-5 for detailed discussion). Given that hyperbolic lattices have been experimentally realized in circuit quantum electrodynamics [1] and electric circuits [2–4], higher-order topological phases in hyperbolic lattices may be observed in these systems. In fact, higher-order topological phases in square lattices have been observed in phononic [45], microwave [46], electric circuit [47], and photonic systems [48]. Our work may also inspire the interest of studying higher-order topological phases in hyperbolic lattices in quantum simulators, such as cold atom systems [49, 50].

We thank J.-H. Wang for helpful discussions. This work is supported by the National Natural Science Foundation of China (Grant No. 11974201) and Tsinghua University Dushi Program..

* yongxuphy@tsinghua.edu.cn

- [1] A. J. Kollár, M. Fitzpatrick, and A. A. Houck, *Nature* **571**, 45 (2019).
- [2] W. Zhang, H. Yuan, N. Sun, H. Sun, and X. Zhang, *Nat. Commun.* **13**, 2937 (2022).
- [3] P. M. Lenggenhager, A. Stegmaier, L. K. Upreti, T. Hofmann, T. Helbig, A. Vollhardt, M. Greiter, C. H. Lee, S. Imhof, H. Brand, T. Kießling, I. Boettcher, T. Neupert, R. Thomale, T. Bzdušek, *Nat. Commun.* **13**, 4373 (2022).
- [4] A. Chen, H. Brand, T. Helbig, T. Hofmann, S. Imhof, A. Fritzsche, T. Kießling, A. Stegmaier, L. K. Upreti, T. Neupert, T. Bzdušek, M. Greiter, R. Thomale, and I. Boettcher, arXiv:2205.05106 (2022).
- [5] A. J. Kollár, M. Fitzpatrick, P. Sarnak, and A. A. Houck, *Commun. Math. Phys.* **376**, 1909 (2019).
- [6] S. Yu, X. Piao, and N. Park, *Phys. Rev. Lett.* **125**, 053901 (2020).
- [7] I. Boettcher, P. Bienias, R. Belyansky, A. J. Kollár, and A. V. Gorshkov, *Phys. Rev. A* **102**, 032208 (2020).
- [8] J. Maciejko and S. Rayan, *Sci. Adv.* **7**, eabe9170 (2021).
- [9] K. Ikeda, S. Aoki, and Y. Matsuki, *J. Phys.: Condens. Matter* **33**, 485602 (2021).
- [10] A. Saa, E. Miranda, and F. Rouxinol, arXiv:2108.08854 (2021).
- [11] J. Maciejko, S. Rayan, *Proc. Natl. Acad. Sci.* **119**, e2116869119 (2022).
- [12] P. Bienias, I. Boettcher, R. Belyansky, A. J. Kollár, and A. V. Gorshkov, *Phys. Rev. Lett.* **128**, 013601 (2022).
- [13] A. Stegmaier, L. K. Upreti, R. Thomale, and I. Boettcher, *Phys. Rev. Lett.* **128**, 166402 (2022).
- [14] I. Boettcher, A. V. Gorshkov, A. J. Kollár, J. Maciejko, S. Rayan, and R. Thomale, *Phys. Rev. B* **105**, 125118 (2022).
- [15] Z.-R. Liu, C.-B. Hua, T. Peng, and B. Zhou, *Phys. Rev. B* **105**, 245301 (2022).
- [16] D. M. Urwyler, P. M. Lenggenhager, I. Boettcher, R. Thomale, T. Neupert, T. Bzdušek, arXiv:2203.07292 (2022).
- [17] N. Cheng, F. Serafin, J. McInerney, Z. Rocklin, K. Sun, and X. Mao, arXiv:2203.15208 (2022).
- [18] W. A. Benalcazar, B. A. Bernevig, and T. L. Hughes, *Science* **357**, 61 (2017).
- [19] M. Sitte, A. Rosch, E. Altman, and L. Fritz, *Phys. Rev. Lett.* **108**, 126807 (2012).
- [20] F. Zhang, C. L. Kane, and E. J. Mele, *Phys. Rev. Lett.* **110**, 046404 (2013).
- [21] R.-J. Slager, L. Rademaker, J. Zaanen, and L. Balents, *Phys. Rev. B* **92**, 085126 (2015).
- [22] J. Langbehn, Y. Peng, L. Trifunovic, F. von Oppen, and P. W. Brouwer, *Phys. Rev. Lett.* **119**, 246401 (2017).
- [23] Z. Song, Z. Fang, and C. Fang, *Phys. Rev. Lett.* **119**, 246402 (2017).
- [24] F. Schindler, A. M. Cook, M. G. Vergniory, Z. Wang, S. S. P. Parkin, B. A. Bernevig, and T. Neupert, *Sci. Adv.* **4**, eaat0346 (2018).
- [25] M. Lin and T. L. Hughes, *Phys. Rev. B* **98**, 241103(R) (2018).
- [26] L. Trifunovic and P. W. Brouwer, *Phys. Rev. X* **9**, 011012 (2019).
- [27] M. Rodriguez-Vega, A. Kumar, and B. Seradjeh, *Phys. Rev. B* **100**, 085138 (2019).
- [28] D. Călugăru, V. Juričić, and B. Roy, *Phys. Rev. B* **99**, 041301(R) (2019).
- [29] D. Varjas, A. Lau, K. Pöyhönen, A. R. Akhmerov, D. I. Pikulin, and I. C. Fulga, *Phys. Rev. Lett.* **123**, 196401 (2019).
- [30] X.-L. Sheng, C. Chen, H. Liu, Z. Chen, Z.-M. Yu, Y. X. Zhao, and S. A. Yang, *Phys. Rev. Lett.* **123**, 256402 (2019).
- [31] A. Agarwala, V. Juričić, and B. Roy, *Phys. Rev. Research* **2**, 012067(R) (2020).
- [32] Y.-B. Yang, K. Li, L.-M. Duan, and Y. Xu, *Phys. Rev. Research* **2**, 033029 (2020).
- [33] R. Chen, C.-Z. Chen, J.-H. Gao, B. Zhou, and D.-H. Xu, *Phys. Rev. Lett.* **124**, 036803 (2020).
- [34] A. Tiwari, M.-H. Li, B. A. Bernevig, T. Neupert, and S. A. Parameswaran, *Phys. Rev. Lett.* **124**, 046801 (2020).
- [35] Q.-B. Zeng, Y.-B. Yang, and Y. Xu, *Phys. Rev. B* **101**, 241104(R) (2020).
- [36] C. Chen, Z. Song, J.-Z. Zhao, Z. Chen, Z.-M. Yu, X.-L. Sheng, and S. A. Yang, *Phys. Rev. Lett.* **125**, 056402 (2020).
- [37] Y.-L. Tao, N. Dai, Y.-B. Yang, Q.-B. Zeng, and Y. Xu, *New J. Phys.* **22**, 103058 (2020).
- [38] Y.-B. Yang, K. Li, L.-M. Duan, and Y. Xu, *Phys. Rev. B* **103**, 085408 (2021).
- [39] C.-A. Li, B. Fu, Z.-A. Hu, J. Li, and S.-Q. Shen, *Phys. Rev. Lett.* **125**, 166801 (2020).
- [40] J.-H. Wang, Y.-B. Yang, N. Dai, and Y. Xu, *Phys. Rev.*

- Lett. **126**, 206404 (2021).
- [41] T.-Y. Fan, W. Yang, H. Cheng, and X.-H. Sun, *Generalized Dynamics of Soft-Matter Quasicrystals: Mathematical Models, Solutions and Applications* (Springer, Singapore, 2022), 2nd ed.
- [42] B. Kang, K. Shiozaki, and G. Y. Cho, Phys. Rev. B **100**, 245134 (2019).
- [43] W. A. Wheeler, L. K. Wagner, and T. L. Hughes, Phys. Rev. B **100**, 245135 (2019).
- [44] In Fig. 2(a), on the right side of the vertical dashed line, there is a tiny plateau region where the energy gap in momentum space is finite. Such a region arises from the edge energy gap closing if we consider open boundaries along the direction of k_1 or k_2 .
- [45] M. Serra-Garcia, V. Peri, R. Süsstrunk, O. R. Bilal, T. Larsen, L. G. Villanueva, and S. D. Huber, Nature (London) **555**, 342 (2018).
- [46] C. W. Peterson, W. A. Benalcazar, T. L. Hughes, and G. Bahl, Nature (London) **555**, 346 (2018).
- [47] S. Imhof, C. Berger, F. Bayer, J. Brehm, L. W. Molenkamp, T. Kiessling, F. Schindler, C. H. Lee, M. Greiter, T. Neupert, and R. Thomale, Nat. Phys. **14**, 925 (2018).
- [48] S. Mittal, V. V. Orre, G. Zhu, M. A. Gorlach, A. Poddubny, and M. Hafezi, Nat. Photonics **13**, 692 (2019).
- [49] D. Barredo, S. de Léséleuc, V. Lienhard, T. Lahaye, and A. Browaeys, Science **354**, 1021 (2016).
- [50] M. Endres, H. Bernien, A. Keesling, H. Levine, E. R. Anschuetz, A. Krajenbrink, C. Senko, V. Vuletić, M. Greiner, and M. D. Lukin, Science **354**, 1024 (2016).

In the Supplemental Material, we will prove that $\bar{Q}_{12} = \bar{Q}_{23} = \bar{Q}_{34} = \bar{Q}_{41}$ in Section S-1, provide more detailed discussion on the band and topological properties of the higher-order topological hyperbolic semimetal phase in the 4D momentum space in Section S-2, show that the reentrant gapped topological phase may arise from finite-size effects in Section S-3, present the effect of weak disorder on topological phases in Section S-4, and finally utilize the corner charge to characterize the gapped topological phases in Section S-5.

S-1. PROOF OF THE RELATION ON THE QUADRUPOLE MOMENT

In this section, we will prove that $\bar{Q}_{12} = \bar{Q}_{23} = \bar{Q}_{34} = \bar{Q}_{41}$, where \bar{Q}_{ij} is the average quadrupole moment defined in Eq. (3) in the main text. The system in Eq. (1) in the main text respects the C_8M_1 symmetry, and with this symmetry, the Hamiltonian $H(\mathbf{k})$ in momentum space satisfies

$$U_{C_8M_1} H(k_1, k_2, k_3, k_4) (U_{C_8M_1})^{-1} = H(-k_4, k_1, k_2, k_3), \quad (\text{S1})$$

where $U_{C_8M_1}$ is a unitary matrix. Fixing parameter momenta (k_3, k_4) and spanning square lattice momenta (k_1, k_2) , we obtain the set of occupied eigenstates $U_{o,12}(k_3, k_4) = (|\psi_1\rangle, |\psi_2\rangle, \dots, |\psi_{n_c}\rangle)$ with $|\psi_j\rangle$ being the j th occupied eigenstate of H_s (one of $n_c = 32L^2$ occupied states). One can obtain the column vector $|\psi_j\rangle$ using the eigenstate of $H(\mathbf{k})$, that is, $[|\psi_j\rangle]_{(nm)} = e^{i\mathbf{k}_{12} \cdot \mathbf{r}_n} [|\psi_\lambda(\mathbf{k})\rangle]_m$, where $\mathbf{k}_{12} \equiv k_1 \mathbf{e}_x + k_2 \mathbf{e}_y$, \mathbf{r}_n denotes the position of the n th unit cell and $|\psi_\lambda(\mathbf{k})\rangle$ is an eigenstate of $H(\mathbf{k})$. For clarity, we write down the definition of the quadruple moment as

$$Q_{12}(k_3, k_4) = \left[\frac{1}{2\pi} \text{Im} \log \det([U_{o,12}(k_3, k_4)]^\dagger \hat{D} U_{o,12}(k_3, k_4)) - Q_o \right] \text{mod } 1, \quad (\text{S2})$$

where we have explicitly indicated that $U_{o,12}$ is a function of k_3 and k_4 .

Thanks to the C_8M_1 symmetry, $U_{C_8M_1} |\psi_\lambda(\mathbf{k})\rangle$ is an eigenstate of $H(-k_4, k_1, k_2, k_3)$. It follows that applying $U_{C_8M_1}^{\oplus L^2}$ (for an $L \times L$ square lattice) to $U_{o,12}(k_3, k_4)$ leads to $U_{o,23}(-k_4, k_3) U_{\text{exc}}$, that is,

$$U_{C_8M_1}^{\oplus L^2} U_{o,12}(k_3, k_4) = U_{o,23}(-k_4, k_3) U_{\text{exc}}, \quad (\text{S3})$$

where in the Hamiltonian $H(k_1, q_2, q_3, k_4)$, k_1 is replaced by $-k_4$ and k_4 is replaced by k_3 . U_{exc} realizes the exchange of column vectors so as to arrange the occupied eigenstates in a certain order (in fact, the order is not important). As a result, we have

$$\begin{aligned} Q_{23}(-k_4, k_3) &= \left\{ \frac{1}{2\pi} \text{Im} \log \det[U_{o,23}^\dagger(-k_4, k_3) \hat{D} U_{o,23}(-k_4, k_3)] - Q_o \right\} \text{mod } 1 \\ &= \left\{ \frac{1}{2\pi} \text{Im} \log \det[U_{\text{exc}} U_{o,12}^\dagger(k_3, k_4) (U_{C_8M_1}^{\oplus L^2})^{-1} \hat{D} U_{C_8M_1}^{\oplus L^2} U_{o,12}(k_3, k_4) U_{\text{exc}}^{-1}] - Q_o \right\} \text{mod } 1 \\ &= \left\{ \frac{1}{2\pi} \text{Im} \log \det[U_{o,12}^\dagger(k_3, k_4) (U_{C_8M_1}^{\oplus L^2})^{-1} \hat{D} U_{C_8M_1}^{\oplus L^2} U_{o,12}(k_3, k_4)] - Q_o \right\} \text{mod } 1. \end{aligned} \quad (\text{S4})$$

Clearly, \hat{D} commutes with the $U_{C_8 M_1}^{\oplus L^2}$, i.e., $[\hat{D}, U_{C_8 M_1}^{\oplus L^2}] = 0$. We thus arrive at

$$\begin{aligned} Q_{23}(-k_4, k_3) &= \left\{ \frac{1}{2\pi} \text{Im} \log \det[U_{o,12}^\dagger(k_3, k_4) \hat{D} U_{o,12}(k_3, k_4)] - Q_o \right\} \bmod 1, \\ &= Q_{12}(k_3, k_4). \end{aligned} \quad (\text{S5})$$

Averaging the quadrupole moment over parameter momenta (k_3, k_4) , we have the following relations:

$$\begin{aligned} \overline{Q}_{12} &= \frac{1}{(2\pi)^2} \int_0^{2\pi} dk_3 \int_0^{2\pi} dk_4 Q_{12}(k_3, k_4) \\ &= \frac{1}{(2\pi)^2} \int_0^{2\pi} dk_3 \int_0^{2\pi} dk_4 Q_{23}(-k_4, k_3) \\ &= \frac{1}{(2\pi)^2} \int_0^{2\pi} dk_1 \int_0^{2\pi} dk_4 Q_{23}(k_1, k_4) \\ &= \overline{Q}_{23}. \end{aligned} \quad (\text{S6})$$

Similarly, one can also prove that $\overline{Q}_{23} = \overline{Q}_{34} = \overline{Q}_{41}$ by choosing different pairs of parameter momenta.

S-2. THE BAND AND TOPOLOGICAL PROPERTIES OF THE SEMIMETAL PHASE IN THE 4D MOMENTUM-SPACE

In this section, we will provide more detailed discussion on the band and topological properties of the higher-order topological hyperbolic semimetal phase in the 4D momentum space. In Fig. S1(a), we plot the gap of $H(\mathbf{k})$ as a function of g in the 4D Brillouin zone for different system sizes. Clearly, the gap of $H(\mathbf{k})$ closes when $g > 1.31$, leading to a gapless phase.

To illustrate the gapless structure in the semimetal phase, we plot the gapless region for $g = 1.35$ in Fig. S1(b) with color denoting k_1 . We find eight degenerate nodes. We also display the distribution of the quadrupole moment Q_{12} in the (k_3, k_4) plane in Fig. S1(c). We see that a part in the Brillouin zone exhibits Q_{12} of 0.5 and the other part has zero Q_{12} , resulting in a fractional value of the average quadrupole moment. The degenerate nodes projected on the (k_3, k_4) plane cannot completely separate topologically nontrivial and trivial regimes. This is due to the fact that a quadrupole topological insulator can undergo phase transitions through edge energy gap closing without involving any bulk energy gap closing [1].

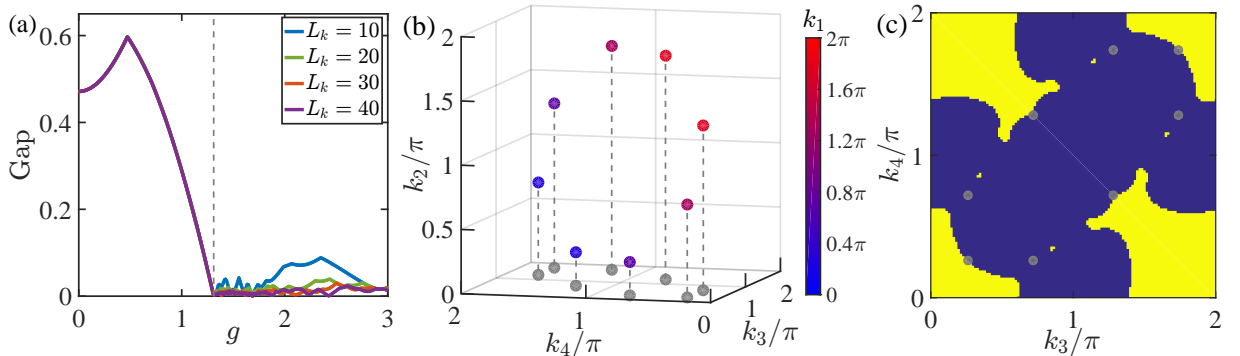


FIG. S1. (a) The energy gap of $H(\mathbf{k})$ with respect to g for different system sizes. The 4D Brillouin zone is spanned by $\{(k_1, k_2, k_3, k_4) | k_i = 2\pi n_i/L_k, n_i = 0, \dots, L_k - 1, i = 1, \dots, 4\}$ with $L_k = 10, 20, 30$, or 40 . (b) The degenerate nodes in the 4D energy spectrum of $H(\mathbf{k})$ with $g = 1.35$. Color denotes the value of the momentum k_1 . Gray nodes are the projection of gapless nodes onto the (k_3, k_4) plane [also see (c)]. (c) The quadrupole moment Q_{12} in the (k_3, k_4) plane for $H(\mathbf{k})$ with $g = 1.35$. In the blue region, $Q_{12} = 0$, whereas in the yellow region, $Q_{12} = 0.5$. Here, $m = 0.8$.

S-3. FINITE-SIZE ANALYSIS

In the main text, we show the existence of a reentrant gapped phase. In the section, we will show that it arises from finite-size effects, which open the gap of edge states while leave the gap of corner modes unchanged.

To elaborate on the effect, we calculate the average proportion p_α of particles on the boundary for the corner modes ($\alpha = c$) and edge modes ($\alpha = e$) by

$$p_\alpha = \frac{1}{N_\alpha} \sum_{i \in S_\alpha} \sum_{\mathbf{r} \in \mathcal{L}} \sum_j |\Psi_{i,j}(\mathbf{r})|^2, \quad (\text{S7})$$

where $\Psi_{i,j}(\mathbf{r})$ is the j th component of the i th occupied eigenstate at site \mathbf{r} of the Hamiltonian in Eq. (1) in the main text under open boundary conditions, and \mathcal{L} denotes a set consisting of boundary sites of the hyperbolic lattice. S_c is a set consisting of four eigenstates with lowest positive energy, which correspond to the corner modes in the topologically nontrivial regime. S_e is a set containing ten eigenstates from the fifth positive energy level to the fourteenth positive level; these modes mainly correspond to the edge modes. N_α denotes the number of elements in S_α .

Figure S2(a) shows that as g enters into the reentrant gapped regime, p_e suddenly drops to a value smaller than N_b/N_{all} , the proportion of boundary sites [N_b is the number of boundary sites and N_{all} is the number of all sites]. It indicates that the edge states may experience some overlap due to finite-size effects so that their distribution in the bulk increases. Indeed, when we increase the system size, such overlap decreases so that the transition point from the gapless phase to the reentrant gapped one also increases, leading to a smaller reentrant regime [see Fig. S2(b) and (c)]. We thus expect that in the thermodynamic limit, the phase may disappear. The other factor accounting for the presence of the phase is that the corner modes are less sensitive to finite-size effects than the edge states, as reflected by Fig. S2(a). There, p_c experiences a significant decline across $g \sim 2$, leading to a finite gap for the corner modes. For comparison, we also plot the energy spectrum of the Hamiltonian in Eq. (1) in the main text on square lattices. We clearly see that only the gapped higher-order topological phase exists. We thus conclude that the specific geometry of hyperbolic lattices not only allows for the existence of higher-order topological phases with the symmetry without crystalline counterpart, but also the appearance of several phase transitions with respect to g .

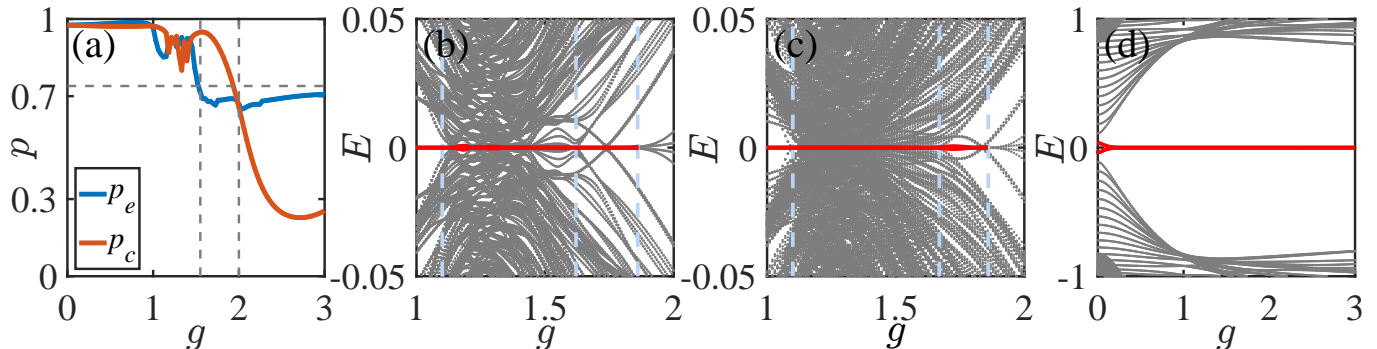


FIG. S2. (a) The average proportion p_α of particles on the boundary for the corner modes $\alpha = c$ and edge modes $\alpha = e$ as a function of g . The system has 768 sites, which is the same as in Fig. 2(b) in the main text. The energy spectrum of the tight-binding Hamiltonian in Eq. (1) in the main text as a function of g under open boundary conditions with (b) 2888 sites, and (c) 10800 sites. Red lines highlight the zero-energy corner modes. The region of reentrant gapped topological phase for the case with 2888 sites is $1.62 \lesssim g \lesssim 1.86$, and the one with 10800 sites is $1.67 \lesssim g \lesssim 1.86$, suggesting that the reentrant region is reduced as the system size increases. In addition, the edge gap of this region also becomes smaller with the increase of the system size. In (a)-(c), the results are for hyperbolic lattices, while in (d), the energy spectrum is for square lattices. Here, $m = 0.8$.

S-4. STABILITY AGAINST DISORDER

In this section, we discuss the effect of weak disorder on topological phases by introducing the on-site disorder mass term

$$H_{\text{dis}} = \sum_{i,\alpha,\beta} m_r W_i |i\alpha\rangle [\tau_z \sigma_0]_{\alpha\beta} \langle i\beta|, \quad (\text{S8})$$

where W_i is a random variable that is uniformly distributed in $[-1, 1]$ respecting C_8 symmetry and m_r is the strength of disorder. This term respects the chiral symmetry and C_8T symmetry, i.e., $[H_{\text{dis}}, \Gamma] = [H_{\text{dis}}, C_8T] = 0$.

To illustrate that the higher-order topological hyperbolic phases are stable against weak disorder, we calculate the local DOS at zero energy averaged over 100 samples in the presence of weak disorder with $m_r = 0.1$. Figure S3 shows that the existence of disorder does not destroy the corner modes, indicating the stability of these topological phases against weak disorder.

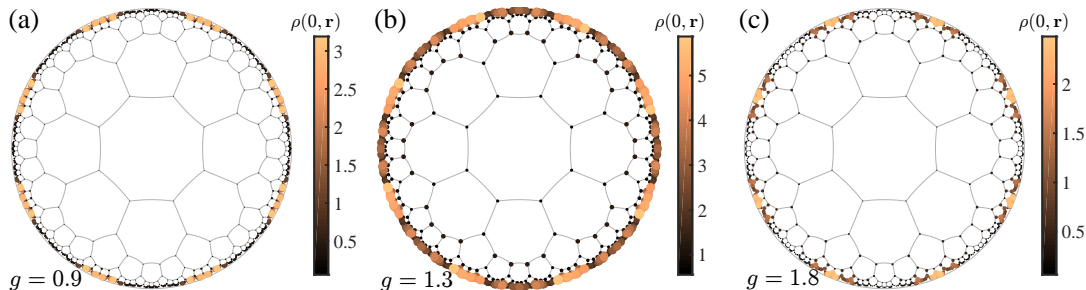


FIG. S3. The sample averaged local DOS at zero energy in the presence of weak disorder with $m_r = 0.1$ for (a) $g = 0.9$, (b) $g = 1.3$ and (c) $g = 1.8$, which correspond to Fig. 3(a-c) in the main text. Here, $m = 0.8$.

S-5. CORNER CHARGE

For gapped topological phases with corner modes, boundary obstructions lead to the corner-localized fractional charges $\pm e/2$ [1, 2]. In our case, such corner charges should appear over a $1/8$ sector $S_{1/8}$ [see Fig. S4(a)]. Therefore, we use the net charge over a sector at half filling to characterize the topological feature of the system in real space, which is defined as

$$C_S = e \left[2N_{S_{1/8}} - \sum_{i \in \text{occ}} \sum_{\mathbf{r} \in S_{1/8}} \sum_j |\Psi_{i,j}(\mathbf{r})|^2 \right], \quad (\text{S9})$$

where $N_{S_{1/8}}$ is the number of sites in this sector and $\Psi_{i,j}(\mathbf{r})$ is the j th component of the i th occupied eigenstate at site \mathbf{r} . The first term arises from the background positive charge over $S_{1/8}$ (each site contributes a $+2e$ charge). To determine the part contributed by electrons, we introduce a small δ -term $H_\delta = \sum_{i,\alpha,\beta} \delta|i\alpha\rangle [\tau_x \sigma_z]_{\alpha\beta} \langle i\beta|$, so that the eightfold degeneracy of the zero-energy states is lifted, leading to four corner states with positive energy and the other four with negative energy. As a result, only four corner states are occupied at half filling.

In Fig. S4(b), we plot C_S with respect to g . In the deep gapped ($0 < g \lesssim 1.1$) and reentrant gapped ($1.55 \lesssim g \lesssim 2$) regimes, $|C_S|$ approaches the quantized value of 0.5, reflecting that these two regimes are topologically nontrivial. Note that when g is small, there is a small gap for the corner modes due to finite-size effects, leading to the inaccurate evaluation of the corner charge. In the gapped trivial phase ($g > 2$), the corner charge declines to zero. Also note that in the gapless region, the corner charge is not a well defined quantity.

* yongxuphy@tsinghua.edu.cn

[S1] Y.-B. Yang, K. Li, L.-M. Duan, and Y. Xu, Phys. Rev. Research **2**, 033029 (2020).

[S2] E. Khalaf, W. A. Benalcazar, T. L. Hughes, and R. Queiroz, Phys. Rev. Research **3**, 013239 (2021).

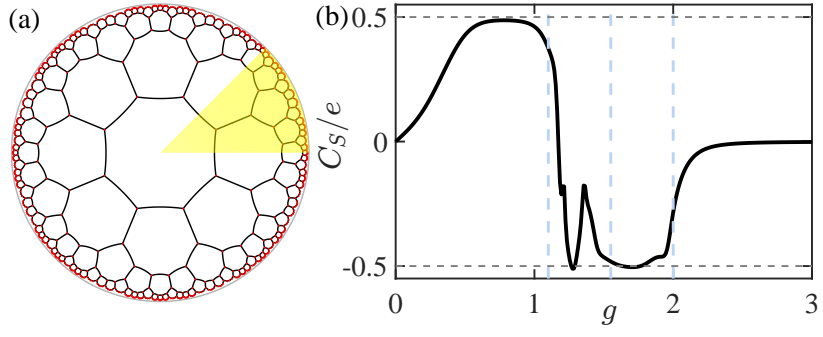


FIG. S4. (a) Schematic of the Poincaré disk model for the hyperbolic $\{8,3\}$ lattice. The yellow region represents the $1/8$ sector $S_{1/8}$. (b) C_S with respect to g for the tight-binding model Hamiltonian in Eq. (1) in the main text with 746 sites. Here, $m = 0.8$.